PHYSICAL REVIEW C **95**, 064319 (2017)

Toroidal, compressive, and $E1$ properties of low-energy dipole modes in ^{10}Be

Yoshiko Kanada-En'yo and Yuki Shikata
Department of Physics, Kyoto University, Kyoto 606-8502, Japan

(Received 18 April 2017; published 22 June 2017)

We studied dipole excitations in ^{10}Be based on an extended version of the antisymmetrized molecular dynamics, which can describe 1p-1h excitations and large amplitude cluster modes. Toroidal and compressive dipole operators are found to be good proves to separate the low-energy and high-energy parts of the isoscalar dipole excitations, respectively. Two low-energy 1^- states, the toroidal dominant 1^-_1 state at $E \sim 8$ MeV and the $E1$ dominant 1^-_2 state at $E \sim 16$ MeV, were obtained. By analysis of transition current densities, the 1^-_1 state is understood as a toroidal dipole mode with exotic toroidal neutron flow caused by rotation of a deformed ^{6}He cluster, whereas the 1^-_2 state is regarded as a neutron-skin oscillation mode, which are characterized by surface neutron flow with inner isoscalar flow caused by the surface neutron oscillation against the 2α core.

DOI: 10.1103/PhysRevC.95.064319

I. INTRODUCTION

In recent developments in physics of unstable nuclei, low-energy dipole excitations have being attracting great interests and intensively studied in experimental and theoretical works (see, e.g., reviews in Refs. [1–4], and references therein). Remarkable progress has been made in these years in experimentally studying isospin characters of low-energy dipole excitations for various nuclei, in particular, neutron-rich nuclei [4–9]. For stable nuclei, familiar dipole excitations in high-energy region known to be giant dipole resonances (GDRs) have been systematically observed in various nuclei by means of photonuclear reactions and α (or ^{6}Li) inelastic scatterings, which can probe isovector (IV) and isoscalar (IS) dipole excitations, respectively [10–14]. The low-energy dipole strengths below the GDR energy are often called as pigmy dipole resonances (PDR) and considered to be new excitation modes decoupled from the GDR modes. In IV dipole ($E1$) excitations, the IV GDR (IVGDR) is understood as the collective vibration mode originating in the opposite oscillation between protons and neutrons. To understand the low-energy $E1$ strengths, a picture of surface neutron oscillation against a core has been proposed. In this paper, we call this mode "neutron-skin oscillation mode". (In some works, the word "PDR" is used to call this specific mode.) Also in IS dipole (ISD) excitations, low-energy strengths known in such nuclei as ^{16}O, ^{40}Ca, and ^{208}Pb [12,15,16] have been discussed in relation to an exotic dipole mode, i.e., the toroidal dipole (TD) mode [1,14,17–23].

The TD mode carries vorticity and its character is much different from the compressive dipole (CD) mode, which is the normal mode for the ISGDR. In this decade, IS and IV properties of low-energy dipole excitations have been intensively studied to clarify essential nature of low-energy dipole modes [1,3,4]. One of the interesting problems is whether the vorticity origin TD mode arises as low-energy resonances in nuclear systems. In works with a quasiparticle phonon model (QPM) and random phase approximation (RPA) for such nuclei as ^{208}Pb and ^{132}Sn [19,21–23], it has been shown that the TD mode dominates the low-energy part of the ISD strengths whereas the CD mode mainly excites the high-energy part for the ISGDR, indicating that the toroidal property is a key for low-energy dipole resonances. The TD dominant nature of the low-energy $E1$ resonances has been demonstrated by toroidal flow in transition current densities [1,18,19,21–23]. In the works of Refs. [22,23], no low-energy $E1$ resonances for the pure neutron-skin oscillation mode has been obtained.

For light stable nuclei, low-energy IS strengths can be good probes also for cluster states [24–36]. As discussed by Yamada *et al.* [29] and Chiba *et al.* [35], cluster states can be strongly excited by IS compressive modes such as IS monopole (ISM) and ISD modes. For instance, in ^{12}C and ^{16}O, the enhanced low-energy ISM strengths are understood as cluster states. Moreover, significant low-energy ISD strengths observed in such nuclei as ^{12}C and ^{16}O [38,39] are considered to probe 1^- cluster states as discussed in Ref. [33].

In light neutron-rich nuclei, a further rich variety of cluster states are expected to appear in excited states because of excess neutrons surrounding clusters (see, for example, Refs. [40–42], and references therein). A typical example is the cluster structures consisting of a 2α-cluster core and surrounding valence neutrons in neutron-rich Be (see also a review in Ref. [43]). The ISM strengths in Be isotopes have been theoretically studied by cluster models and suggested to be a good probe for cluster states [43–45]. One of the authors, Y.K-E., has studied the $E1$ and compressive ISD strengths of Be isotopes and discussed the dipole excitations for cluster states [46].

Our main aim is to investigate toroidal nature of the low-energy dipole excitations in ^{10}Be. We are going to show how the toroidal, compressive, and $E1$ operators excite low-energy cluster states and high-energy GDRs. A particular attention is paid on two components, the toroidal and the neutron-skin oscillation modes, in the low-energy dipole strengths for cluster states.

Usually, either a mean-field approach or a cluster model fails to describe low-energy cluster states and high-energy GRs in a unified manner because cluster states are large amplitude modes of highly correlated many nucleons beyond mean-field approaches, whereas GR modes are collective vibrations described by coherent 1p-1h excitations, which are not contained in ordinary cluster model space. To take into account large amplitude cluster modes and coherent 1p-1h excitations, we have recently developed a new method based on the antisymmetrized molecular dynamics (AMD) [42,47–51]: the shifted-basis AMD (sAMD) combined with the cluster generator coordinate method (GCM) [32,33,46]. In the method, we superpose various configurations including 1p-1h and cluster states expressed by AMD wave functions. In the framework, angular-momentum and parity projections are microscopically performed and the center-of-mass motion is exactly removed. The method has been applied to investigate ISM excitations in ^{16}O and ISM and ISD in ^{12}C, and proved to be a useful method to describe monopole and dipole excitations in a wide energy region including low-energy cluster modes and higher-energy GR modes in a unified framework. In our previous work [46], we applied the method for $E1$ and ISD excitations in neutron-rich Be isotopes and showed that low-energy $E1$ and ISD strengths for cluster states appear separating from high-energy strengths for GDRs. In this paper, we investigate toroidal, compressive, and $E1$ properties of dipole excitations in ^{10}Be based on reanalysis of the previous calculation. By analysis of transition current densities in the low-energy dipole excitations, we show a toroidal feature of cluster states. We also perform a cluster model analysis to obtain intuitive understanding of toroidal dominance in the 1_1^- state and $E1$ dominance in the 1_2^- states.

This paper is organized as follows. The definition of dipole operators and transitions are explained in Sec. II. The calculation scheme and results of dipole excitations in ^{10}Be are shown in Sec. III, and properties of low-energy dipole modes are discussed in Sec. IV. The paper concludes with a summary and an outlook in Sec. V. In the Appendixes, we explain definitions of operators and matrix elements.

II. DEFINITIONS OF TD, CD, AND $E1$ OPERATORS AND STRENGTHS

Vortical nature of nuclear current has been discussed for a long time (see, e.g., a review in Ref. [21]). However, the definition of vorticity in nuclear systems has yet to be confirmed. To measure the nuclear vorticity, two different modes have been proposed. One is the mode originally determined by the second-order correction in the long-wave approximation of the transition $E\lambda$ operator in an electromagnetic field [52,53], and the other is that defined based on multipole decomposition of the transition current density following Ravenhall-Wambach's prescription [54]. In Ref. [21], they call the former and the latter, the toroidal and vortical modes, respectively, and described the general treatment of toroidal, compressive, and vortical modes and their relation to each other. In this paper, we basically follow the descriptions of the TD, CD, and vortical dipole (VD) operators in Ref. [21].

The TD, CD, and VD operators are defined as

$$M_{\mathrm{TD}}(\mu) = \frac{-i}{2\sqrt{3}c}\int d\boldsymbol{r}\,\boldsymbol{j}(\boldsymbol{r}) \cdot \left[\frac{\sqrt{2}}{5}r^2\boldsymbol{Y}_{12\mu}(\hat{\boldsymbol{r}}) + r^2\boldsymbol{Y}_{10\mu}(\hat{\boldsymbol{r}})\right], \tag{1}$$

$$M_{\mathrm{CD}}(\mu) = \frac{-i}{2\sqrt{3}c}\int d\boldsymbol{r}\,\boldsymbol{j}(\boldsymbol{r}) \cdot \left[\frac{2\sqrt{2}}{5}r^2\boldsymbol{Y}_{12\mu}(\hat{\boldsymbol{r}}) - r^2\boldsymbol{Y}_{10\mu}(\hat{\boldsymbol{r}})\right], \tag{2}$$

$$M_{\mathrm{VD}}(\mu) = \frac{-i}{2\sqrt{3}c}\int d\boldsymbol{r}\,\boldsymbol{j}(\boldsymbol{r}) \cdot \left[\frac{3\sqrt{2}}{5}r^2\boldsymbol{Y}_{12\mu}(\hat{\boldsymbol{r}})\right], \tag{3}$$

where $\boldsymbol{j}(\boldsymbol{r})$ is the current density operator and $\boldsymbol{Y}_{\lambda L\mu}$ is the vector spherical harmonics. Note that $M_{\mathrm{VD}} = M_{\mathrm{TD}} + M_{\mathrm{CD}}$. In this paper, we take into account only the convection part of the nuclear current but skip its magnetization (spin) part. The definition of $\boldsymbol{j}(\boldsymbol{r})$ as well as that of density $\rho(\boldsymbol{r})$ are given in Appendix A. The term $\boldsymbol{Y}_{10\mu}(\hat{\boldsymbol{r}})$ includes the $L = 1$ excitation of the center-of-mass motion, but it gives no contribution to the transition matrix element in the AMD framework because the center-of-mass motion of the AMD wave function is fixed to be an S-wave state and can be exactly removed.

The TD operator can be written using a curl of the transition current density as $M_{\mathrm{TD}} \propto \int d\boldsymbol{r}(\nabla \times \boldsymbol{j}) \cdot (r^3\boldsymbol{Y}_{11\mu})$, and the CD operator, $M_{\mathrm{CD}} \propto \int d\boldsymbol{r}(\nabla \cdot \boldsymbol{j})r^3 Y_{1\mu}$, is regarded as the counter part of the TD operator. In a hydrodynamical sense, the TD and CD modes are considered to be vortical and irrotational, respectively. On the other hand, the VD operator measures the $\boldsymbol{Y}_{12\mu}$ component of the transition current $\boldsymbol{j}$ and free from the $\boldsymbol{Y}_{10\mu}$ component. In the Ravenhall-Wambash's prescription [54], $\boldsymbol{Y}_{\lambda\lambda+1\mu}$ and $\boldsymbol{Y}_{\lambda\lambda-1\mu}$ components of $\boldsymbol{j}$ are interpreted as vortical and irrotational parts. In their definition, the VD operator is vortical, whereas the TD and CD operators are mixed modes of both vortical ($\boldsymbol{Y}_{\lambda\lambda+1\mu}$) and irrotational ($\boldsymbol{Y}_{\lambda\lambda-1\mu}$) components. Kvasil and his collaborators argued that the TD operator is a natural measure of the nuclear vorticity [21,22], though there exist studies with the TD operator and those with the VD one. They demonstrated with RPA calculations that the TD operator is a good mode to separate the low-energy dipole mode from the high-energy CD mode.

For a dipole transition from the ground state, $|0\rangle \to |f\rangle$, matrix elements of these operators are written with the transition current density $\delta\boldsymbol{j}(\boldsymbol{r}) \equiv \langle f|\boldsymbol{j}(\boldsymbol{r})|0\rangle$ as

$$\langle f|M_{\mathrm{TD}}(\mu)|0\rangle = \frac{-i}{2\sqrt{3}c}\int d\boldsymbol{r}\delta\boldsymbol{j}(\boldsymbol{r}) \cdot \left[\frac{\sqrt{2}}{5}r^2\boldsymbol{Y}_{12\mu}(\hat{\boldsymbol{r}}) + r^2\boldsymbol{Y}_{10\mu}(\hat{\boldsymbol{r}})\right], \tag{4}$$

$$\langle f|M_{\mathrm{CD}}(\mu)|0\rangle = \frac{-i}{2\sqrt{3}c}\int d\boldsymbol{r}\delta\boldsymbol{j}(\boldsymbol{r}) \cdot \left[\frac{2\sqrt{2}}{5}r^2\boldsymbol{Y}_{12\mu}(\hat{\boldsymbol{r}}) - r^2\boldsymbol{Y}_{10\mu}(\hat{\boldsymbol{r}})\right], \tag{5}$$

$$\langle f|M_{\mathrm{VD}}(\mu)|0\rangle = \frac{-i}{2\sqrt{3}c}\int d\boldsymbol{r}\delta\boldsymbol{j}(\boldsymbol{r}) \cdot \left[\frac{3\sqrt{2}}{5}r^2\boldsymbol{Y}_{12\mu}(\hat{\boldsymbol{r}})\right]. \tag{6}$$

By using the continuity equation

$$\nabla\cdot\boldsymbol{j}=-\frac{i}{\hbar}[H,\rho], \tag{7}$$

the matrix element of the CD operator is straightforwardly transformed to that of the familiar IS dipole ($IS1$) operator as

$$\langle f|M_{\rm CD}(\mu)|i\rangle=-\frac{1}{10}\frac{E}{\hbar c}\langle f|M_{IS1}(\mu)|i\rangle, \tag{8}$$

$$M_{IS1}(\mu)\equiv\int d\boldsymbol{r}\rho(\boldsymbol{r})r^3Y_{1\mu}(\hat{\boldsymbol{r}}), \tag{9}$$

where E is the excitation energy $E\equiv E_f-E_0$ given with the initial energy (E_0) and final energy (E_f). The $E1$ operator is written with the IV density operator $\rho^{\rm IV}(\boldsymbol{r})$ as

$$M_{E1}(\mu)\equiv\int d\boldsymbol{r}\rho^{\rm IV}(\boldsymbol{r})rY_{1\mu}(\hat{\boldsymbol{r}}), \tag{10}$$

and also written with the IV current density operator $\boldsymbol{j}^{\rm IV}(\boldsymbol{r})$ as

$$M_{E1}(\mu)=-\frac{i\hbar}{E}\sqrt{\frac{3}{4\pi}}\int d\boldsymbol{r}j^{\rm IV}_{\mu}(\boldsymbol{r}). \tag{11}$$

The transition strength for a dipole operator $M_{\rm D}$ is given as

$$B({\rm D};0\to f)=\frac{1}{2J_0+1}|\langle f|M_{\rm D}|0\rangle|^2, \tag{12}$$

where J_0 is the angular momentum of the initial state. We define scaled strengths of the TD, VD, and CD transitions

$$\tilde{B}(\text{TD,VD,CD})=\left(\frac{10\hbar c}{E}\right)^2B(\text{TD,VD,CD}), \tag{13}$$

so that $\tilde{B}$(CD) corresponds to the ordinary ISD strength $B(IS1)$.

III. DIPOLE EXCITATIONS OF ^{10}Be

A. Calculation scheme of sAMD + αGCM

We calculate the ground and 1^- states of ^{10}Be with the sAMD combined with the α-cluster GCM (αGCM). The sAMD method with the GCM has been constructed and applied for study of ISM, ISD, and $E1$ excitations in light nuclei such as ^{12}C and ^{16}O, and neutron-rich Be [32,33,46]. For the detailed scheme of the present calculation of ^{10}Be, the reader is referred to the previous paper [46]. A similar method has been recently applied to study $E1$ and ISD excitations in ^{26}Ne by Kimura [37].

In the AMD framework, a basis wave function is given by a Slater determinant,

$$\Phi_{\rm AMD}(\boldsymbol{Z})=\frac{1}{\sqrt{A!}}\mathcal{A}\{\varphi_1,\varphi_2,\ldots,\varphi_A\}, \tag{14}$$

where $\mathcal{A}$ is the antisymmetrizer, and φ_i is the ith single-particle wave function written by a product of spatial, spin, and isospin wave functions as

$$\varphi_i=\phi_{\boldsymbol{X}_i}\chi_i\tau_i, \tag{15}$$

$$\phi_{\boldsymbol{X}_i}(\boldsymbol{r}_j)=\left(\frac{2\nu}{\pi}\right)^{3/4}\exp[-\nu(\boldsymbol{r}_j-\boldsymbol{X}_i)^2], \tag{16}$$

$$\chi_i=\left(\frac{1}{2}+\xi_i\right)\chi_\uparrow+\left(\frac{1}{2}-\xi_i\right)\chi_\downarrow, \tag{17}$$

where $\phi_{\boldsymbol{X}_i}$ and χ_i are the spatial and spin functions, respectively, and τ_i is the isospin function fixed to be proton or neutron. The width parameter ν is chosen to be $\nu=0.19$ fm^{-2} so as to minimize the ground state energy of ^{10}Be. The condition

$$\frac{1}{A}\sum_{i=1,\ldots,A}\boldsymbol{X}_i=0 \tag{18}$$

is kept for all basis AMD wave functions so that the center-of-mass motion can be exactly separated from the total wave function. An AMD wave function is specified by a set of variational parameters, $\boldsymbol{Z}\equiv\{\boldsymbol{X}_1,\ldots,\boldsymbol{X}_A,\xi_1,\ldots,\xi_A\}$, for centroids of single-nucleon Gaussian wave packets and spin orientations of all nucleons.

To obtain the wave function for the lowest J^π state, we perform variation after projections (VAP) with the AMD wave function. Namely, the parameters $\boldsymbol{Z}$ are determined by the energy variation after the angular-momentum and parity projections,

$$\frac{\delta}{\delta\boldsymbol{X}_i}\frac{\langle\Phi|H|\Phi\rangle}{\langle\Phi|\Phi\rangle}=0, \tag{19}$$

$$\frac{\delta}{\delta\xi_i}\frac{\langle\Phi|H|\Phi\rangle}{\langle\Phi|\Phi\rangle}=0, \tag{20}$$

$$\Phi=P^{J\pi}_{MK}\Phi_{\rm AMD}(\boldsymbol{Z}), \tag{21}$$

where $P^{J\pi}_{MK}$ is the angular-momentum and parity projection operator. For ^{10}Be, the variation is performed after the $J^\pi=0^+$ and $J^\pi=1^-$ projections to obtain the wave functions for the ground and the lowest 1^- states, respectively. We denote the obtained parameter set $\boldsymbol{Z}$ for the ground state as $\boldsymbol{Z}^0_{\rm VAP}=\{\boldsymbol{X}^0_1,\ldots,\xi^0_1,\ldots\}$, and those for the 1^-_1 state as $\boldsymbol{Z}^{1^-_1}_{\rm VAP}$.

To take into account 1p-1h excitations on the ground state, we consider a small variation of single-particle wave functions of $\Phi_{\rm AMD}(\boldsymbol{Z}^0_{\rm VAP})$ by shifting the Gaussian centroid of the ith single-particle wave function, $\boldsymbol{X}^0_i\to\boldsymbol{X}^0_i+\epsilon\boldsymbol{e}_\sigma$, where ϵ is an enough small constant and $\boldsymbol{e}_\sigma$ ($\sigma=1,\ldots,8$) are unit vectors for eight directions defined in the previous paper. For the spin part of the shifted single-particle wave function, the spin-nonflip and spin-flip states given by parameters ξ^0_i and $\bar{\xi}^0_i=-1/(4\xi^0_i)^*$ are adopted. In the sAMD method, totally $16A$ wave functions of the spin-nonflip and spin-flip shifted AMD wave functions with the parameters

$$\boldsymbol{Z}^0_{\rm s}(i,\sigma)\equiv\{\boldsymbol{X}^{0\prime}_1,\cdots,\boldsymbol{X}^{0\prime}_i+\epsilon\boldsymbol{e}_\sigma,\cdots,\boldsymbol{X}^{0\prime}_A,\\ \xi^0_1,\cdots,\xi^0_i,\cdots,\xi^0_A\}, \tag{22}$$

$$\boldsymbol{Z}^0_{\bar{\rm s}}(i,\sigma)\equiv\{\boldsymbol{X}^{0\prime}_1,\cdots,\boldsymbol{X}^{0\prime}_i+\epsilon\boldsymbol{e}_\sigma,\cdots,\boldsymbol{X}^{0\prime}_A,\\ \xi^0_1,\cdots,\bar{\xi}^0_i,\cdots,\xi^0_A\} \tag{23}$$

are adopted as basis wave functions in addition to the original ground state wave function $\Phi_{\mathrm{AMD}}(\mathbf{Z}^0_{\mathrm{VAP}})$. Here, we take into account the recoil effect and choose $\boldsymbol{X}^{0\prime}_j = \boldsymbol{X}^0_j - \epsilon \boldsymbol{e}_\sigma/(A-1)$ to keep the condition (18).

As discussed in the previous paper, the ^{10}Be ground state obtained by the AMD+VAP shows a ^{6}He + α cluster structure with an intercluster distance $D_0 = 2.8$ fm even though any clusters are not *a priori* assumed in the AMD framework. To take into account large amplitude intercluster motion, we apply the αGCM by changing the intercluster distance (the α-cluster distance from ^{6}He) $D_0 \to D_0 + \Delta D$. We label the parameter set as $\mathbf{Z}^0_\alpha(\Delta D)$, which is specified by the shift ΔD of the intercluster distance. The basis wave functions given by $\mathbf{Z}^0_\alpha(\Delta D)$ ($\Delta D = -1,0,1,\dots,19,20$ fm) are superposed in the αGCM.

Finally, we combine the sAMD and αGCM by superposing all the basis wave functions in addition to the VAP wave functions, $\Phi_{\mathrm{AMD}}(\mathbf{Z}^0_{\mathrm{VAP}})$ and $\Phi_{\mathrm{AMD}}(\mathbf{Z}^{1^-_1}_{\mathrm{VAP}})$. Consequently, the final wave functions for the 0^+_1 and 1^-_k states are given as

$$\begin{aligned}\Psi\big(J^\pi_k\big) = {} & \sum_K c_0\big(J^\pi_k;K\big) P^{J\pi}_{MK} \Phi_{\mathrm{AMD}}\big(\mathbf{Z}^0_{\mathrm{VAP}}\big) \\ & + \sum_K c_1\big(J^\pi_k;K\big) P^{J\pi}_{MK} \Phi_{\mathrm{AMD}}\big(\mathbf{Z}^{1^-_1}_{\mathrm{VAP}}\big) \\ & + \sum_{i=1,\dots,A} \sum_\sigma \sum_K c_2\big(J^\pi_k;i,\sigma,K\big) \\ & \times P^{J\pi}_{MK} \Phi_{\mathrm{AMD}}\big(\mathbf{Z}^0_{\mathrm{s}}(i,\sigma)\big) \\ & + \sum_{i=1,\dots,A} \sum_\sigma \sum_K c_3\big(J^\pi_k;i,\sigma,K\big) \\ & \times P^{J\pi}_{MK} \Phi_{\mathrm{AMD}}\big(\mathbf{Z}^0_{\bar{\mathrm{s}}}(i,\sigma)\big) \\ & + \sum_{\Delta D} \sum_K c_4\big(J^\pi_k;\Delta D,K\big) \\ & \times P^{J\pi}_{MK} \Phi_{\mathrm{AMD}}\big(\mathbf{Z}^0_\alpha(\Delta D)\big), \end{aligned} \tag{24}$$

where coefficients c_i are determined by diagonalization of the norm and Hamiltonian matrices. Note that the present calculation corresponds to that labeled as "sAMD + αGCM + cfg" in the previous paper.

For the dipole excitations $0^+_1 \to 1^-_k$, the transition strength of a dipole operator M_D are calculated with the obtained sAMD + αGCM wave functions, $\Psi(J^\pi_k)$, as

$$B(D;0^+_1 \to 1^-_k) = |\langle \Psi(1^-_k)|M_D|\Psi(0^+_1)\rangle|^2. \tag{25}$$

In the present framework of the sAMD+αGCM, the ground state is obtained by the VAP, and therefore, it contains correlations such as cluster correlations beyond mean field approximation. Moreover, 1p-1h excitations on the ground state are taken into account in the sAMD model space, and also large amplitude cluster motion is treated by means of the αGCM.

B. Effective interactions

The adopted effective interaction is the same as that used in the previous paper. It consists of the central force of the MV1 force [55] and the spin-orbit term of the G3RS force [56,57]. The MV1 force is given by two-range Gaussian two-body terms and a zero-range three-body term. For parametrization of the MV1 force, case 1 with the Bartlett, Heisenberg, and Majorana parameters, $b = h = 0$ and $m = 0.62$, is used. As for strengths of the G3RS spin-orbit force with a two-range Gaussian form, $u_I = -u_{II} \equiv u_{ls} = 3000$ MeV are used. This set of interaction parameters describes well properties of the ground and excited states of ^{10}Be and ^{12}C with the AMD+VAP calculations [58–60]. For matter properties, the MV1 force with the present parameters gives the saturation density $\rho_s = 0.192$ fm^{-3}, the saturation energy $E_s = -17.9$ MeV, the effective nucleon mass $m^*_{\mathrm{SNM}} = 0.59\,m$ for symmetric nuclear and $m^*_{\mathrm{PNM}} = 0.80\,m$ for pure neutron matters, the incompressibility $K = 245$ MeV, the symmetry energy $S = 37.6$ MeV, and the slope parameter of the symmetry energy $L = 47.7$ MeV.

C. Results of ^{10}Be calculated with sAMD + αGCM

Dipole strengths

Energy-weighted dipole strength distributions obtained with the sAMD + αGCM are shown in Fig. 1. The calculated results for ordinary IS and IV dipole, i.e., CD ($IS1$) and $E1$ strengths correspond to those shown in the previous paper. In the $E1$ excitations [see Fig. 1(d)], a remarkable low-energy strength at $E = 16$ MeV [23% of the Thomas-Reiche-Kuhn (TRK) sum rule] appears below the IVGDR energy because of valence neutron motion against the 2α core. The IVGDR strengths in $E \geqslant 20$ MeV originate in the 2α-core $E1$, namely, opposite oscillations between protons and neutrons in the 2α core part. Because of the prolate deformation of the 2α core, the IVGDR shows a two-peak structure, the narrow peak at $E \sim 25$ MeV for the the longitudinal mode and the broad bump around $E \sim 40$ MeV for the transverse mode, which is largely fragmented because of the coupling with the valence neutron motion. In the CD excitations [see Fig. 1(a)], the broad strengths for the ISGDR are obtained in $E = 25$–50 MeV region, relatively higher energy than the IVGDR. Below the ISGDR, the low-energy CD strengths with 2% of the ISD sum rule [12] are obtained.

ISD strengths for the TD and VD modes are compared with the CD mode in Fig. 1(a). In contrast to the CD mode which strongly excites the ISGDR in the high-energy region, the TD strengths are dominantly distributed in the low-energy region rather than the high energy region. The VD mode excites both the low-energy and high-energy dipole resonances. It means that the TD and CD operators are suitable to separately probe the low-energy and high-energy parts of the ISD excitations, respectively, whereas the VD operator may not be a good probe to decouple the low-energy and high-energy modes. This result is consistent with the result of the RPA calculation for ^{208}Pb [21]. The proton and neutron contributions in the CD and TD strengths are shown in Figs. 1(b) and 1(c). In the CD excitations, the proton contribution dominates the strength at $E = 16$ MeV and also that around $E \sim 50$ MeV, whereas the neutron contribution is significant for the strength around $E \sim 40$ MeV. In the TD excitations, a remarkable strength at $E = 8$ MeV comes from the neutron part.

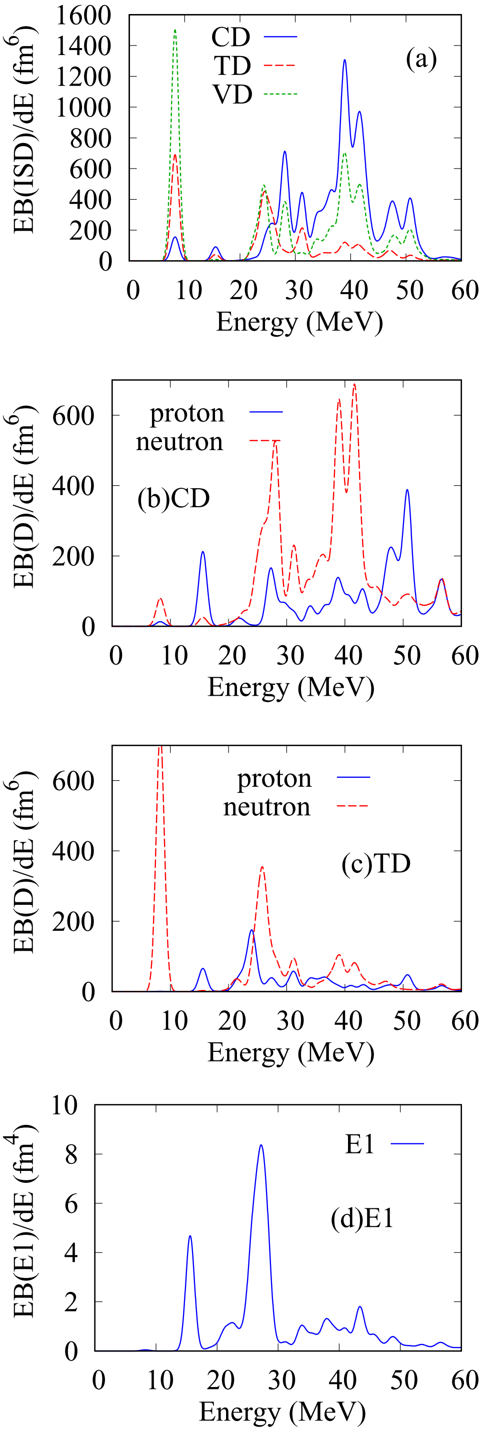

FIG. 1. Energy-weighted dipole strengths $E\tilde{B}(\mathrm{CD}), E\tilde{B}(\mathrm{TD})$, $E\tilde{B}(\mathrm{VD})$, and $EB(E1)$ for the CD, TD, VD, and E1 modes of ^{10}Be calculated with the sAMD+αGCM. The proton and neutron contributions in the CD and TD modes are shown in (b) and (c). The smearing width is $\gamma = 1$ MeV.

Let us discuss the low-energy dipole excitations in $E \leqslant 20$ MeV. Two 1^- resonances are obtained at $E = 8$ MeV and $E = 16$ MeV. In this paper, we call the lower and higher ones the 1^-_1 $(E = 8$ MeV) and 1^-_2 $(E = 16$ MeV), which were labeled as "B1" and"B2" in the previous paper, respectively. In the $E1$ mode, the transition to the 1^-_1 almost vanishes, whereas that to the 1^-_2 is remarkably strong. In the CD mode, the strengths for both the 1^-_1 and 1^-_2 are not so enhanced but visible in the strength distribution. In the TD mode, the 1^-_1 has a remarkably strong TD transition, but the 1^-_2 shows a relatively weak TD transition. Thus, two low-energy dipole excitations show quite different transition properties; the TD dominance in the 1^-_1 and the $E1$ dominance in the 1^-_2.

It should be noted that the 1^-_1 state has large overlap with the the VAP wave function and corresponds to the band-head state of the $K = 1$ band assigned to the experimental 1^-_1 state at 5.960 MeV as discussed in the work with the AMD+VAP in Ref. [59]. The calculated $B(E1; 1^-_1 \to 0^+_1)$ value is as small as 1.1×10^{-2} W.u., which is almost consistent with the theoretical value 7.9×10^{-3} W.u. calculated by a molecular orbital model [61]. The experimental $B(E1; 1^-_1 \to 0^+_1)$ reported in Ref. [62] is in the range of 5.4×10^{-5} to 1.1×10^{-3}. Our result of the weak $E1$ transition for the 1^-_1 is qualitatively supported by the experimental data, but it one-order overestimates the experimental $B(E1)$. There is no experimental information for the 1^-_2.

IV. PROPERTIES OF LOW-ENERGY DIPOLE MODES OF ^{10}Be

As discussed previously, we obtain two low-energy dipole excitations, the TD dominant 1^-_1 and $E1$ dominant 1^-_2. Such a difference in the transition properties may indicate the coexistence of two kinds of low-energy dipole modes. In this section, we discuss properties of the low-energy dipole excitations focusing on toroidal features. At first, we discuss intrinsic structures and transition current densities based on analysis of the AMD wave functions. Next we perform an analysis using a simple cluster model of $^6\mathrm{He} + \alpha$ to obtain intuitive understanding of the dipole modes.

A. Structures and transition current densities for the 1^-_1 and 1^-_2 states in the intrinsic frame

The sAMD + αGCM wave functions, $\Psi(0^+_1)$ and $\Psi(1^-_1)$, for the ground and 1^-_1 states, have more than 90% overlap with the J^π-projected VAP wave functions, $P^{0+}_{00}\Phi_{\mathrm{AMD}}(\boldsymbol{Z}^0_{\mathrm{VAP}})$ and $P^{1-}_{MK=1}\Phi_{\mathrm{AMD}}(\boldsymbol{Z}^{1^-_1}_{\mathrm{VAP}})$, respectively. Therefore, $\Phi_{\mathrm{AMD}}(\boldsymbol{Z}^0_{\mathrm{VAP}})$ and $\Phi_{\mathrm{AMD}}(\boldsymbol{Z}^{1^-_1}_{\mathrm{VAP}})$ are regarded as approximate intrinsic wave functions for the ground and 1^-_1 states. Since each AMD wave function before the projections is expressed by a single Slater determinant, we can investigate intrinsic structure of each state in the intrinsic (body-fixed) frame. We choose the intrinsic frame XYZ with the principal axes, which satisfy $\langle Y^2\rangle \leqslant \langle X^2\rangle \leqslant \langle Z^2\rangle$ and $\langle XY\rangle = \langle YZ\rangle = \langle ZX\rangle = 0$. Here the expectation values are defined for the intrinsic state without the projections.

The intrinsic proton and neutron densities of $\Phi_{\mathrm{AMD}}(\boldsymbol{Z}^0_{\mathrm{VAP}})$ and $\Phi_{\mathrm{AMD}}(\boldsymbol{Z}^{1^-_1}_{\mathrm{VAP}})$ are shown in Fig. 2. It is found that the 0^+_1 and 1^-_1 show a 2α core with two neutrons. One of the α clusters and two neutrons compose a deformed ^{6}He cluster, which is placed in the transverse orientation on the Z axis at

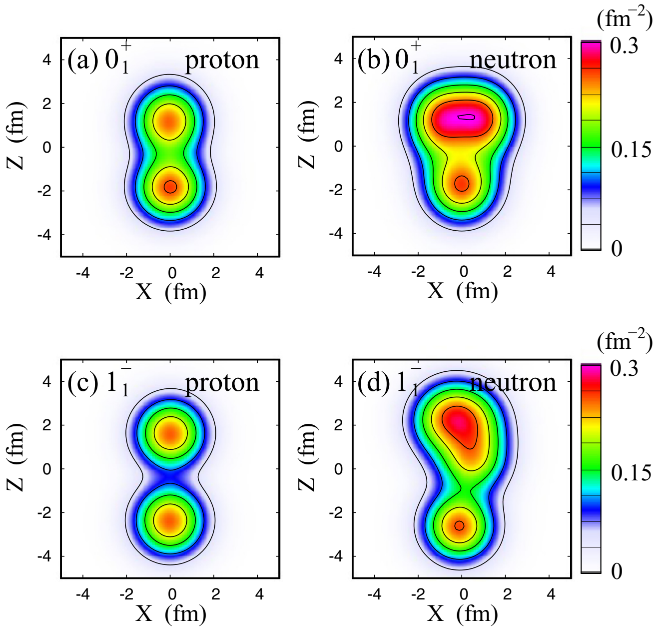

FIG. 2. Intrinsic density distributions of protons and neutrons in ^{10}Be(0_1^+) and ^{10}Be(1_1^-) obtained with the AMD+VAP calculation. Density integrated along the Y axis is plotted on the X-Z plane.

the ^{6}He-α distance $D = 2.8$ fm in the 0_1^+, and in the tilted (rotated) orientation at $D = 3.9$ fm in the 1_1^-.

The 1_2^- state has significant overlap with the αGCM basis wave functions $P^{J\pi}_{MK=0}\Phi_{\rm AMD}(\boldsymbol{Z}^0_\alpha(\Delta D))$ indicating that it arises from the inter-cluster (^{6}He-α) excitation from the ground state. As shown in Fig. 3, $\Psi(1_2^-)$ has the maximum overlap at $D = 3.8$ fm ($\Delta D = 1$ fm) somewhat larger than the distance $D_0 = 2.8$ fm of the ground state. In the following analysis, we simply consider the basis AMD wave function $\Phi_{\rm AMD}(\boldsymbol{Z}^0_\alpha(\Delta D))$ at the maximum overlap as an approximate intrinsic wave function for the 1_2^- state, though it has 60% overlap with $\Psi(1_2^-)$ at most.

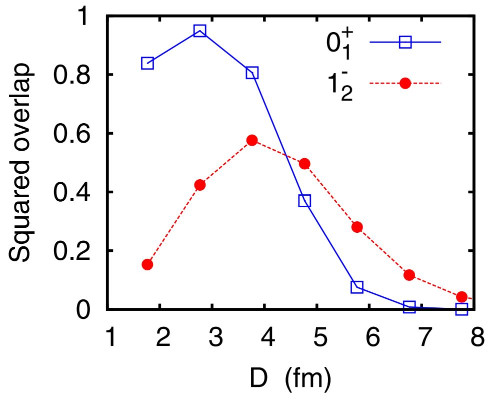

FIG. 3. Squared overlap of $\Psi(J_k^\pi)$ with the αGCM basis wave functions $P^{J\pi}_{M0}\Phi_{\rm AMD}(\boldsymbol{Z}^0_\alpha(\Delta D))$. The overlaps for $\Psi(0_1^+)$ and $\Psi(1_2^-)$ are plotted as functions of the ^{6}He-α distance ($D = D_0 + \Delta D$).

We label the parity eigenstates projected from these approximate intrinsic wave functions as

$$|0^+_{1,\rm int}\rangle \equiv P^+\Phi_{\rm AMD}\big(\boldsymbol{Z}^0_{\rm VAP}\big), \tag{26}$$

$$|1^-_{1,\rm int}\rangle \equiv P^-\Phi_{\rm AMD}\big(\boldsymbol{Z}^{1_1^-}_{\rm VAP}\big), \tag{27}$$

$$|1^-_{2,\rm int}\rangle \equiv P^-\Phi_{\rm AMD}\big(\boldsymbol{Z}^0_\alpha(\Delta D{=}1\text{ fm})\big). \tag{28}$$

Using the parity-projected intrinsic wave functions, we calculate the transition current densities,

$$\delta\boldsymbol{j}(X,Y,Z) = \langle 1^-_{k,\rm int}|\boldsymbol{j}|0^+_{1,\rm int}\rangle, \tag{29}$$

in the intrinsic frame. The calculated $\delta\boldsymbol{j}(X,Y,Z)$ for $|0^+_{1,\rm int}\rangle \to |1^-_{1,\rm int}\rangle$ and $|0^+_{1,\rm int}\rangle \to |1^-_{2,\rm int}\rangle$ at $Y = 0$ on the X-Z plane are shown in Figs. 4 and 5. As seen in Figs. 4(a) and 4(d), the transition current density for $|0^+_{1,\rm int}\rangle \to |1^-_{1,\rm int}\rangle$ shows toroidal neutron flow induced by the ^{6}He-cluster rotation (see schematic figures in Fig. 6). In contrast, the transition current density for $|0^+_{1,\rm int}\rangle \to |1^-_{2,\rm int}\rangle$ (Fig. 5) shows no toroidal feature but translational flow parallel to the Z axis, namely, surface neutron flow with inner isoscalar flow caused by the valence neutron oscillation against the 2α core, which is regarded as the neutron-skin oscillation mode [see Fig. 6(e)].

These transition current densities describe characteristics of the low-energy dipole excitations, i.e., the TD dominance in the 1_1^- and the $E1$ dominance in the 1_2^-. In the transition $0_1^+ \to 1_1^-$, the toroidal current gives significant contribution to the TD strength but it gives no contribution to the $E1$ strength because it does not contain the translational mode. On the other hand, in the transition $0_1^+ \to 1_2^-$ arising from the valence neutron motion against the 2α core, the 2α motion contributes only to the IS component but not to the IV component. Therefore, the surface neutron current simply enhances the $E1$ strength. By contrast, in the IS component, the contribution of the surface neutron current is canceled by the opposite inner IS current. As a result of this cancellation by the recoil effect from the core, the TD transition is weak in $0_1^+ \to 1_2^-$.

B. Properties of dipole modes based on ^{6}He + α-cluster model analysis

In the present result of ^{10}Be, we obtain the remarkable $E1$ strength for the 1_2^- state because of the valence neuron motion against the 2α core. This corresponds to the neutron-skin oscillation mode, which has been expected to appear in low-energy $E1$ strength of neutron-rich nuclei. For the 1_2^- state, the TD strength almost vanishes because of the cancellation of the surface neutron current and the inner IS current of the recoiled core. The vanishing of the TD strength is not trivial because the neutron-skin oscillation mode could contain some toroidal component through the neutron flow along the surface. Indeed, the transition current density in $0_1^+ \to 1_2^-$ shows such the surface neutron flow, which is naively expected to somewhat contribute to the TD strength if the opposite contribution from the recoiled core is absent. Moreover, there is no obvious reason why the CD strength for the 1_2^- state is visible in the CD strength distribution compared with the TD strength. Unfortunately, at a glance on the transition current densities, it is not easy to understand quantitatively the cancellation

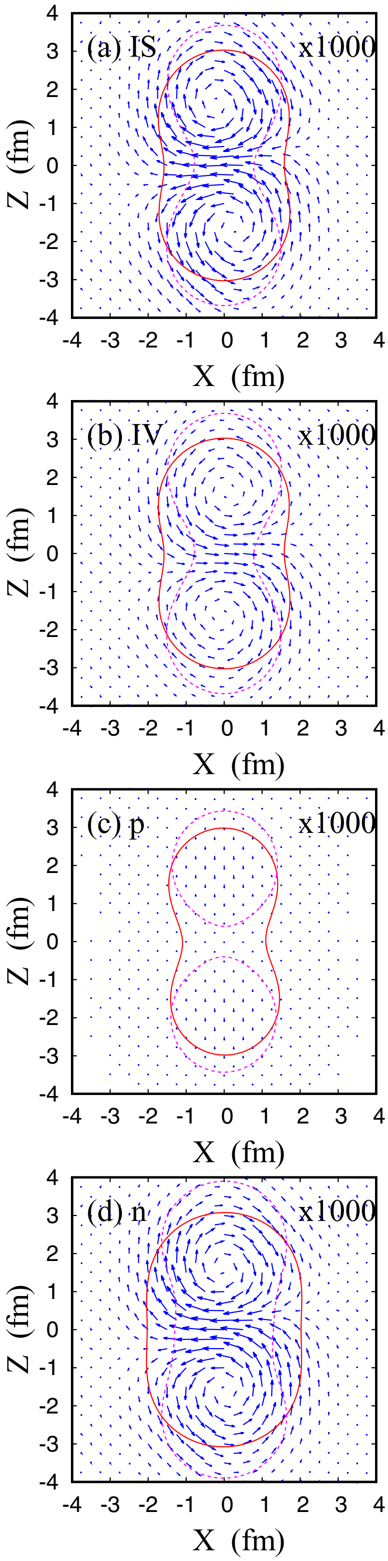

FIG. 4. Vector plots of the transition current densities for $|0^+_{1,\rm int}\rangle \rightarrow |1^-_{1,\rm int}\rangle$. (a) IS, (b) IV, (c) proton, and (d) neutron transition current densities ($c$fm^{-3} unit) at $Y = 0$ are plotted on the X-Z plane (scaled by a factor of 10^3). Red solid (magenta dashed) lines in (a) and (b) show contours for the matter density $\rho(X,0,Z) = 0.08$ fm^{-3} of $|0^+_{1,\rm int}\rangle$ ($|1^-_{1,\rm int}\rangle$), and those in (c) and (d) show contours for the proton and neutron densities $\rho_{p,n}(X,0,Z) = 0.04$ fm^{-3}, respectively.

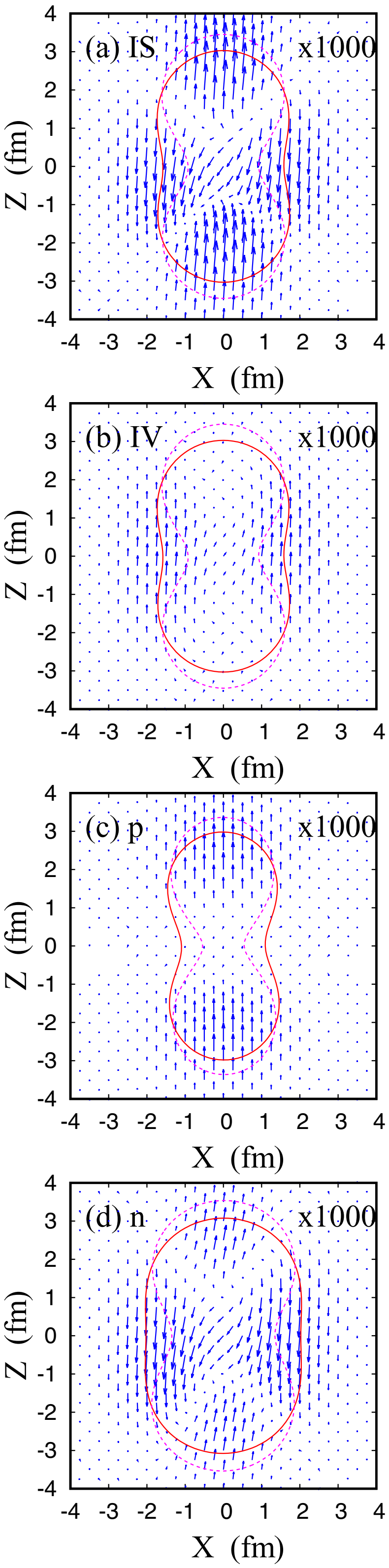

FIG. 5. Same as Fig. 4 but for $|0^+_{1,\rm int}\rangle \rightarrow |1^-_{2,\rm int}\rangle$.

between the valence neutron and core contributions in the TD strength.

To discuss essential properties of the TD and CD components in $0^+_1 \rightarrow 1^-_1$ and $0^+_1 \rightarrow 1^-_2$, we simply consider ^{6}He + α-

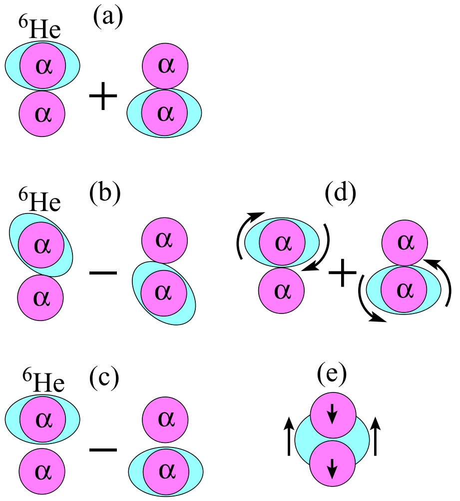

FIG. 6. Schematic figures of (a) ^{10}Be(0^+_1), (b) ^{10}Be(1^-_1), and (c) ^{10}Be(1^-_2), (d) transition current in $0^+_1 \to 1^-_1$, and (e) that in $0^+_1 \to 1^-_2$.

cluster model wave functions instead of the AMD wave functions and analyze detailed contributions of transition current density to the TD and CD strengths in the strong coupling picture. We here introduce the parity-projected Brink-Bloch (BB) cluster wave functions of ^{6}He + α clustering,

$$\Phi^{\pi}_{\rm BB}(\beta;D)=\frac{1}{n_0}P^{\pi}\mathcal{A}\left[\Phi^{\beta}_{^6{\rm He}}(\boldsymbol{S}_1)\Phi_{\alpha}(\boldsymbol{S}_2)\right], \tag{30}$$

$$\boldsymbol{S}_1=\left(0,0,\frac{2}{5}D\right), \tag{31}$$

$$\boldsymbol{S}_2=\left(0,0,-\frac{3}{5}D\right), \tag{32}$$

where n_0 is the normalization factor determined by the condition $|\Phi^{\pi}_{\rm BB}(\beta;D)|=1$, and $\Phi^{\beta}_{^6{\rm He}}(\boldsymbol{S})$ and $\Phi_{\alpha}(\boldsymbol{S})$ are ^{6}He- and α-cluster wave functions given by the harmonic oscillator (h.o.) shell model $(0s)^4p^2$ and $(0s)^4$ configurations localized around the position $\boldsymbol{S}$. β is the label for the valence neutron configuration in p shell. We label p_x^2 (transverse) configuration as $\beta=C_{\rm T}$, and $[(p_x-p_z)/\sqrt{2}]^2$ (rotated) one as $\beta=C_{\rm R}$. In short, we denote $\Phi^{+}_{\rm BB}(C_{\rm T})$, $\Phi^{-}_{\rm BB}(C_{\rm R})$, and $\Phi^{-}_{\rm BB}(C_{\rm T})$ as "$C^+_{\rm T}$", "$C^-_{\rm R}$", and "$C^-_{\rm T}$", which correspond to the intrinsic states of the 0^+_1,1^-_1, and 1^-_2, respectively. Schematic figures for these three configurations are drawn in Figs. 6(a)–6(c). In the present analysis, we take the h.o. width $\nu=0.19$ fm^{-1} and the inter-cluster distance $D=3$ fm.

These wave functions have planer configurations restricted on the X-Z plane, and therefore they are suitable to discuss essential features of the transition current densities projected onto the X-Z plane. The transition current densities for $C^+_{\rm T} \to C^-_{\rm R}$ and $C^+_{\rm T} \to C^-_{\rm T}$ are shown in Figs. 7 and 8, respectively. The transition, $C^+_{\rm T} \to C^-_{\rm R}$, shows the toroidal current similar to that found in $|0^+_{1,\rm int}\rangle \to |1^-_{1,\rm int}\rangle$, and $C^+_{\rm T} \to C^-_{\rm T}$ shows the translational current similarly to $|0^+_{1,\rm int}\rangle \to |1^-_{2,\rm int}\rangle$.

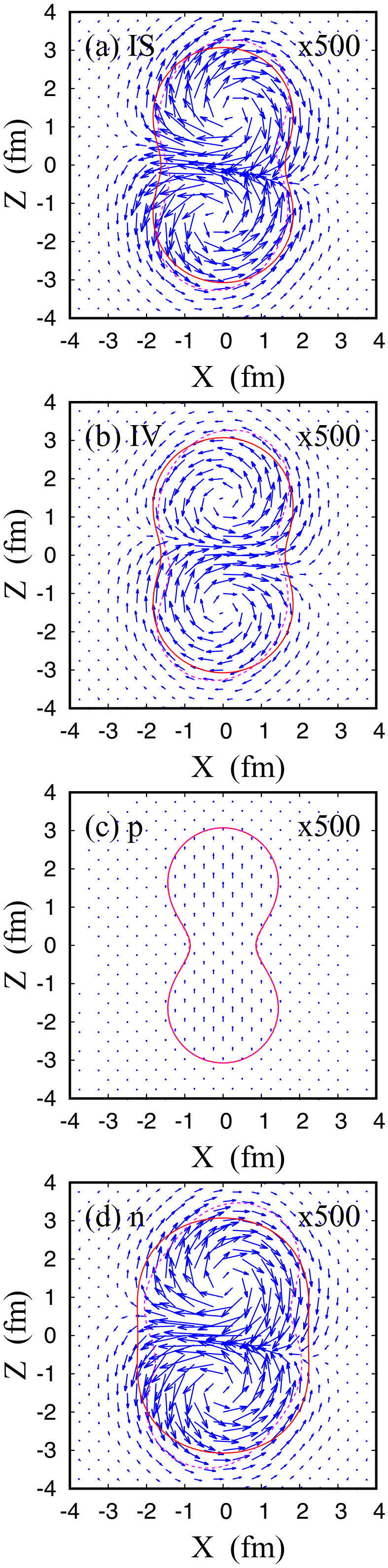

FIG. 7. Same as Fig. 4 but calculated for $C^+_{\rm T} \to C^-_{\rm R}$ with the ^{6}He + α cluster model at $D=3$ fm. The current densities ($c$fm^{-3} unit) are scaled by a factor of 500.

Let us discuss detailed contributions of the transition current densities to the TD and CD modes in the intrinsic frame. For this aim, we define K components of the TD and CD operators in the intrinsic frame, $M_{\rm TD,CD}(K=0)$ and $M_{\rm TD,CD}(|K|=1)$.

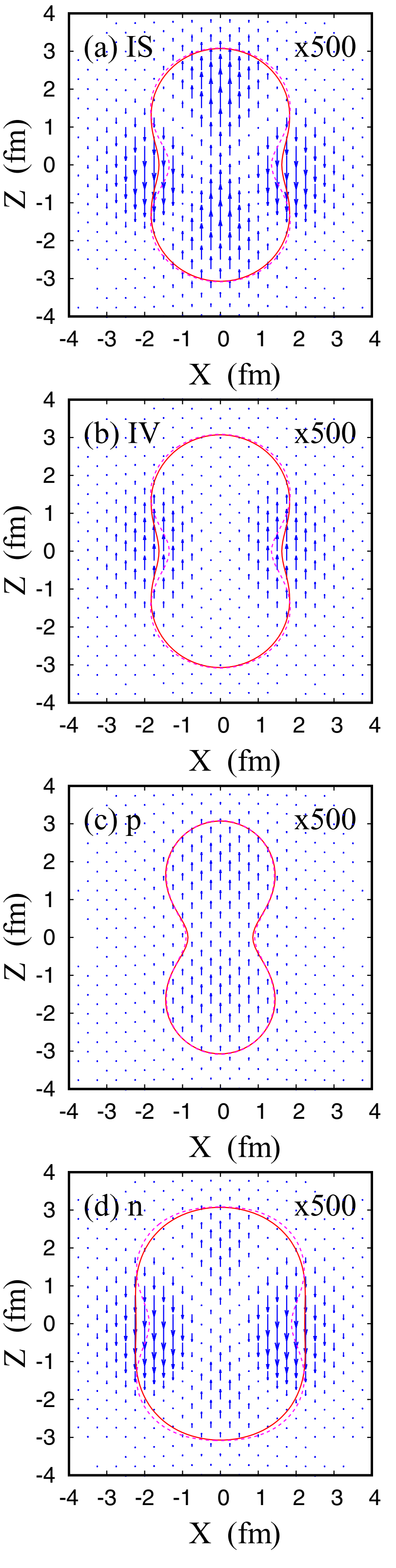

FIG. 8. Same as Fig. 4 but calculated for $C_{\mathrm{T}}^{+} \to C_{\mathrm{T}}^{-}$ with the $^{6}\mathrm{He} + \alpha$ cluster model at $D = 3$ fm. The current densities ($c\mathrm{fm}^{-3}$ unit) are scaled by a factor of 500.

The definition and explicit notation of $M_{\mathrm{TD,CD}}(K = 0)$ and $M_{\mathrm{TD,CD}}(|K| = 1)$ are given in Appendix B. In the strong coupling picture, the TD and CD transition matrix elements are proportional to the integration of the following TD and CD transition densities at $Y = 0$ on the X-Z plane,

$$\mathcal{M}_{\mathrm{TD}}^{K=0}(X,0,Z) = \frac{-i}{20c}\sqrt{\frac{3}{\pi}} \times (2X^2\delta j_Z + Z^2\delta j_Z - ZX\delta j_X), \tag{33}$$

$$\mathcal{M}_{\mathrm{CD}}^{K=0}(X,0,Z) = \frac{-i}{20c}\sqrt{\frac{3}{\pi}} \times (-X^2\delta j_Z - 3Z^2\delta j_Z - 2ZX\delta j_X), \tag{34}$$

$$\mathcal{M}_{\mathrm{TD}}^{|K|=1}(X,0,Z) = \frac{-i}{20c}\sqrt{\frac{3}{\pi}} \times (2Z^2\delta j_X + X^2\delta j_X - XZ\delta j_Z), \tag{35}$$

$$\mathcal{M}_{\mathrm{CD}}^{|K|=1}(X,0,Z) = \frac{-i}{20c}\sqrt{\frac{3}{\pi}} \times (-Z^2\delta j_X - 3X^2\delta j_X - 2XZ\delta j_Z), \tag{36}$$

meaning that $\mathcal{M}_{\mathrm{TD,CD}}^{K}$ can be decomposed into three terms.

For $C_{\mathrm{T}}^{+} \to C_{\mathrm{R}}^{-}$ corresponding to $0_1^+ \to 1_1^-$, we consider the $K = 1$ transition because of the $K = 1$ feature of the 1_1^- state. As given in Eq. (35), the ratio of weight factors of three terms $Z^2\delta j_X, X^2\delta j_X$, and $XZ\delta j_Z$ in the TD mode is $2 : 1 : -1$, which indicates that $Z^2\delta j_X$ is the major term. Similarly, $X^2\delta j_X$ is the major term in the $K = 1$ CD mode. The $K = 1$ component of the TD and CD transition densities for $C_{\mathrm{T}}^{+} \to C_{\mathrm{R}}^{-}$ and its decomposition are shown in Figs. 9 and 10. Clearly seen in the decomposition, the TD transition is enhanced because of remarkable contribution from the $Z^2 j_X$ term [Fig. 10(e)]. In addition, the $XZ\delta j_Z$ term [Fig. 10(d)] gives coherent contribution to the TD transition. Consequently, the TD transition is remarkably strong for $0_1^+ \to 1_1^-$. However, the CD transition is not enhanced because of the cancellation between positive and negative contributions in the major term, $X^2\delta j_X$ [Fig. 10(c)]. Moreover, further cancellation is caused by decoherent contribution from the $Z^2 j_X$ term [Fig. 10(e)].

For $C_{\mathrm{T}}^{+} \to C_{\mathrm{T}}^{-}$ corresponding to $0_1^+ \to 1_2^-$, we consider the $K = 0$ transition because of the $K = 0$ feature of the 1_2^- state. As given in Eqs. (33) and (34), the major terms of the TD and CD modes are $X^2\delta j_Z$ and $Z^2\delta j_Z$, respectively. The $K = 0$ component of the TD and CD transition densities for

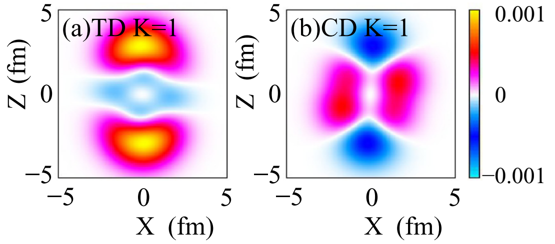

FIG. 9. $|K| = 1$ component of (a) TD and (b) CD transition densities $[(-i)\mathrm{cfm}^{-1}]x$ at $Y = 0$ on the X-Z plane for $C_{\mathrm{T}}^{+} \to C_{\mathrm{R}}^{-}$.

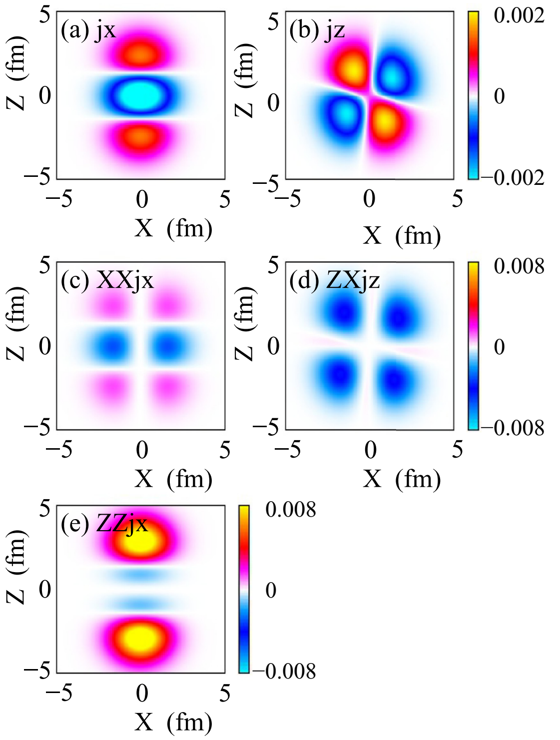

FIG. 10. Decomposition of the $|K| = 1$ component of the transition current densities for $C_{\rm T}^+ \to C_{\rm R}^-$. Non-weighted transition current densities, (a) j_X and (b) j_Z (cfm^{-3}), and the weighted transition current densities, (c) $X^2 j_X$, (d) $XZ j_Z$, and (e) $Z^2 j_X$ (cfm^{-1}), at $Y = 0$ are plotted on the X-Z plane.

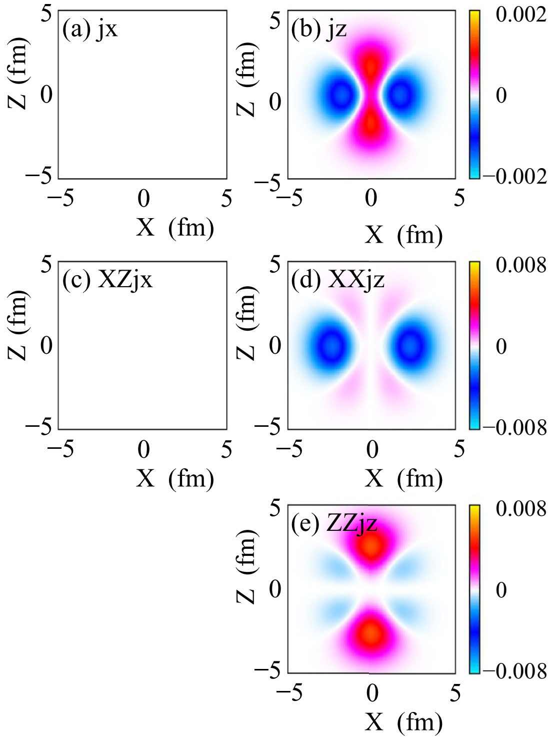

FIG. 12. Decomposition of the $K = 0$ component of the transition current densities for the transition $C_{\rm T}^+ \to C_{\rm T}^-$. Nonweighted transition current densities, (a) j_X and (b) j_Z (cfm^{-3}), and the weighted transition current densities, (c) $ZX j_X$, (d) $XX^2 j_Z$, and (e) $ZZ j_Z$ (cfm^{-1}), at $Y = 0$ are plotted on the X-Z plane.

$C_{\rm T}^+ \to C_{\rm T}^-$ and its decomposition are shown in Figs. 11 and 12. As seen in Fig. 11(a), the TD transition almost vanishes because of the cancellation between positive contribution from the 2α core part and the negative contribution from valence neutrons in the TD transition density. In the decomposition of the TD transition density, the $X^2 J_Z$ and $Z^2 J_Z$ terms cancel each other, whereas the ZXJ_X term vanishes itself. Note that the factor X^2 in $X^2 J_Z$ enhances the surface neutron contribution and the factor Z^2 in $Z^2 J_Z$ enhances the 2α core contribution. It means that the TD transition is suppressed because the contribution of the surface neutron current is canceled by the recoil effect of the 2α core. Also in the CD transition, the $Z^2 J_Z$ (surface neutron) contribution is somewhat canceled by the $X^2 J_Z$ (core) contribution. However, since the $Z^2 J_Z$ term dominates the $K = 0$ component of the CD mode with the factor of 3, the surface neutron contribution remains in the CD mode. As a result, the neutron-skin oscillation mode in $0_1^+ \to 1_2^-$ contains almost no TD component but some CD component.

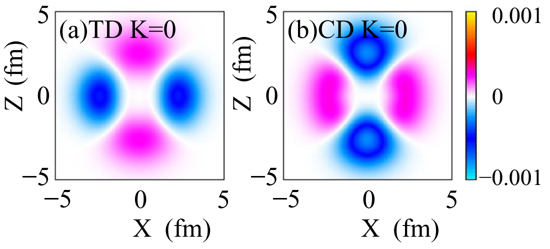

FIG. 11. $K = 0$ component of (a) TD and (b) CD transition current densities [$(-i)$cfm^{-1}] at $Y = 0$ on the X-Z plane for $C_{\rm T}^+ \to C_{\rm T}^-$.

Based on the present analysis of the transition current densities in the intrinsic frame, we can obtain the following understanding of transition current contributions to the TD, CD, and $E1$ strengths. The $0_1^+ \to 1_1^-$ transition is characterized by the toroidal neutron current. In particular, the surface neutron current in the longitudinal part gives significant contribution to the $K = 1$ TD mode [Fig. 13(a)]. On the other hand, the toroidal neutron current gives small contribution to the $K = 1$ CD mode because of the cancellation in the side region [Fig. 13(b)]. The $0_1^+ \to 1_2^-$ transition is characterized by the surface neutron and inner IS currents along the Z axis, which are induced by opposite oscillation between valence neutrons and the 2α core. In the $K = 0$ TD mode, the contribution of the inner IS current from the core part cancels that of the surface neutron current in the side region [Fig. 13(c)]. In the $K = 0$ CD mode, the longitudinal part of the IS current from the recoiled core gives some contribution [Fig. 13(d)]. In the $E1$ mode, the surface neutron current along the Z axis simply contributes to the $E1$ strength without cancellation by the core IS current [Fig. 13(e)].

It should be commented that the BB cluster model wave functions reach to shell-model wave functions in a small limit of the intercluster distance. The shell model limit of $C_{\rm T}^+$ is the $(000)^4(001)^4(100)^2$ configuration. Here, $(n_x n_y n_z)$ is the

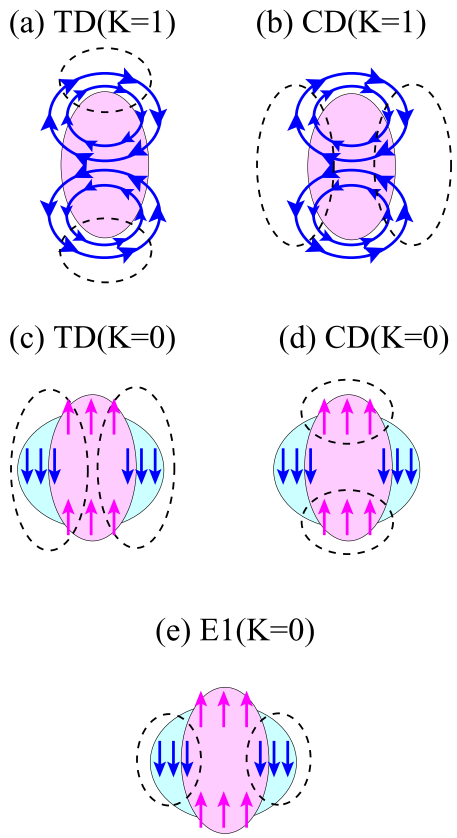

FIG. 13. Schematic figures for transition current densities and their contributions to TD, CD, and $E1$ strengths. (a),(b) Contributions of the toroidal current to $K = 1$ component of the TD and CD modes in $0_1^+ \to 1_1^-$. (c),(d),(e) Contributions of the translational current to $K = 0$ component of the TD, CD, and $E1$ modes in $0_1^+ \to 1_2^-$.

notation for oscillator quanta of single-particle orbits in a h.o. potential. The shell model limit of C_{R}^- is dominated by the $(000)^4(001)^4(100)(002)$ configuration, which corresponds to the 1p-1h excitation, $(100)^{-1}(002)^1$ on the vacuum state $(000)^4(001)^4(100)^2$. Strictly speaking, it also contains additional 1p-1h configurations because of the recoil effect along the Z axis, but they do not contribute to the $|K| = 1$ dipole excitations. The shell model limit of C_{T}^- is expressed by a linear combination of $(100)^{-1}(101)^1$ and $(001)^{-1}(002)^1$ excitations on the vacuum state. The former is neutron excitation, and the latter is the core recoil effect and gives IS contributions (coherent proton and neutron contributions).

V. SUMMARY AND OUTLOOK

We studied dipole excitations in ^{10}Be based on the sAMD + αGCM calculation. The present model takes into account 1p-1h excitations and large amplitude cluster modes, and is useful to describe low-energy dipole strengths for cluster modes and high-energy ones for GDRs. It should be stressed that the parity and angular-momentum projections are performed and the center-of-mass motion can be exactly separated in the present model.

By calculations of the TD, CD, $E1$ strengths, the toroidal and compressive properties of the ISD excitations as well as the $E1$ property have been investigated. It was found that the TD and CD modes dominate the low-energy and high-energy parts of the ISD strengths, respectively. It indicates that the toroidal operator is a good mode to probe the low-energy dipole resonances separately from the ISGDR.

In the low-energy region $E \leqslant 20$ MeV, we obtained two 1^- states, the TD dominant 1_1^- state at $E = 8$ MeV and the $E1$ dominant 1_2^- state at $E = 16$ MeV. The $0_1^+, 1_1^-$, and 1_2^- states have cluster structures with a 2α core and two neutrons regarded as the ^{6}He + α clustering. The $0_1^+ \to 1_1^-$ excitation is interpreted as rotation mode of the deformed ^{6}He cluster, whereas the $0_1^+ \to 1_2^-$ excitation arises from the intercluster (^{6}He-α) motion. The transition current density for $0_1^+ \to 1_1^-$ shows the toroidal neutron flow caused by the ^{6}He-cluster rotation. In contrast, that for $0_1^+ \to 1_2^-$ shows no toroidal feature but the surface neutron flow with the inner IS flow caused by the surface neutron oscillation against the 2α core, i.e., the neutron-skin oscillation mode. These properties of transition current densities describe the TD dominance in the 1_1^- and the $E1$ dominance in the 1_2^-.

We obtained the weak $E1$ for the 1_1^- and predicted the strong $E1$ for the 1_2^-. The 1_1^- state corresponds to the band-head state of the $K = 1$ band and is assigned to the experimental 1_1^- state at 5.960 MeV. Our result of the weak $E1$ transition for the 1_1^- is qualitatively supported by the experimental data, but it one-order overestimates the experimental $B(E1)$. Such the weak $E1$ strength is determined by tiny components of the 1_1^- state. More detailed description of the 1_1^- state might be necessarily to describe the experimental $B(E1)$ value. For the 1_2^-, there is no experimental information. Future experiments to observe the remarkable $E1$ strength for the predicted 1_2^- are requested.

In ^{10}Be, valence neutron motion around the axial symmetric core is essential for the low-energy dipole modes. The coexistence of two different modes, the toroidal mode and the neutron-skin oscillation one, in the low-energy region might be related to decoupling of the $K = 1$ and $K = 0$ dipole modes in the deformed system. An interesting question is whether such phenomena generally appear in deformed neutron-rich nuclei. It is also interesting to search for TD dominant states caused by rotation of a deformed cluster in other nuclei. Experimentally, there is no established method to directly measure TD strengths in unstable nuclei. Analysis of hadronic scatterings based on a reliable reaction theory might be a promising tool.

ACKNOWLEDGMENTS

The computational calculations of this work were performed by using the supercomputer in the Yukawa Institute for theoretical physics, Kyoto University. This work was supported by JSPS KAKENHI Grant No. 26400270.

APPENDIX A: DENSITY AND CURRENT DENSITY OPERATORS

The density and current density operators for nuclear matter are defined as

$$\rho(\boldsymbol{r}) = \sum_k \delta(\boldsymbol{r} - \boldsymbol{r}_k), \tag{A1}$$

$$\boldsymbol{j}(\boldsymbol{r}) = -\frac{i\hbar}{2m} \sum_k \nabla_k \delta(\boldsymbol{r} - \boldsymbol{r}_k) + \delta(\boldsymbol{r} - \boldsymbol{r}_k)\nabla_k. \tag{A2}$$

The current considered here is the convective part of the nuclear current but does not contain the magnetization (spin) part. The transition current density for $|0\rangle \rightarrow |f\rangle$ is defined as

$$\delta \boldsymbol{j}(\boldsymbol{r}) = \langle f|\boldsymbol{j}(\boldsymbol{r})|0\rangle. \tag{A3}$$

The IV, proton, and neutron components are

$$\rho^{\mathrm{IV}}(\boldsymbol{r}) = \frac{N}{A}\rho^{p}(\boldsymbol{r}) - \frac{Z}{A}\rho^{n}(\boldsymbol{r}), \tag{A4}$$

$$\rho^{p(n)}(\boldsymbol{r}) = \sum_{k\in p(n)} \delta(\boldsymbol{r}-\boldsymbol{r}_k), \tag{A5}$$

$$\boldsymbol{j}^{\mathrm{IV}}(\boldsymbol{r}) = \frac{N}{A}\boldsymbol{j}^{p}(\boldsymbol{r}) - \frac{Z}{A}\boldsymbol{j}^{n}(\boldsymbol{r}), \tag{A6}$$

$$\begin{aligned}\boldsymbol{j}^{p(n)} &= -\frac{i\hbar}{2m}\sum_{k\in p(n)} \\ &\quad \times [\nabla_k\delta(\boldsymbol{r}-\boldsymbol{r}_k) + \delta(\boldsymbol{r}-\boldsymbol{r}_k)\nabla_k],\end{aligned} \tag{A7}$$

$$\delta\boldsymbol{j}^{\mathrm{IV}}(\boldsymbol{r}) = \frac{N}{A}\delta\boldsymbol{j}^{p}(\boldsymbol{r}) - \frac{Z}{A}\delta\boldsymbol{j}^{n}(\boldsymbol{r}), \tag{A8}$$

$$\delta\boldsymbol{j}^{p(n)}(\boldsymbol{r}) = \langle f|\boldsymbol{j}^{p(n)}(\boldsymbol{r})|0\rangle. \tag{A9}$$

APPENDIX B: TRANSITIONS IN INTRINSIC FRAME

We define the $K=0$ and $K=1$ components of the TD and CD operators in the intrinsic (body-fixed) frame, XYZ, as

$$M_{\mathrm{TD,CD}}(K=0) \equiv M_{\mathrm{TD,CD}}(\mu=0), \tag{B1}$$

$$\begin{aligned}M_{\mathrm{TD,CD}}(|K|=1) \equiv -\frac{1}{\sqrt{2}}[&M_{\mathrm{TD,CD}}(\mu=+1) \\ &- M_{\mathrm{TD,CD}}(\mu=-1)].\end{aligned} \tag{B2}$$

In the strong-coupling picture, the $K=0$ and $|K|=1$ transitions for $|0_{\mathrm{int}}\rangle \rightarrow |f_{\mathrm{int}}\rangle$ are expressed as

$$\begin{aligned}&\langle f_{\mathrm{int}}|M_{\mathrm{TD,CD}}(K=0,|K|=1)|0_{\mathrm{int}}\rangle \\ &\quad = \int d\boldsymbol{r}_{\mathrm{int}}\mathcal{M}^{K=0,|K|=1}_{\mathrm{TD,CD}}(\boldsymbol{r}_{\mathrm{int}})\end{aligned} \tag{B3}$$

with

$$\begin{aligned}\mathcal{M}^{K=0}_{\mathrm{TD}}(\boldsymbol{r}_{\mathrm{int}}) = \frac{-i}{20c}\sqrt{\frac{3}{\pi}}[&2(X^2+Y^2)\delta j_Z + Z^2\delta j_Z \\ &- ZX\delta j_X - ZY\delta j_Y],\end{aligned} \tag{B4}$$

$$\begin{aligned}\mathcal{M}^{K=0}_{\mathrm{CD}}(\boldsymbol{r}_{\mathrm{int}}) = \frac{-i}{20c}\sqrt{\frac{3}{\pi}}[&-(X^2+Y^2)\delta j_Z - 3Z^2\delta j_Z \\ &- 2ZX\delta j_X - 2ZY\delta j_Y],\end{aligned} \tag{B5}$$

$$\begin{aligned}\mathcal{M}^{|K|=1}_{\mathrm{TD}}(\boldsymbol{r}_{\mathrm{int}}) = \frac{-i}{20c}\sqrt{\frac{3}{\pi}}[&2(Y^2+Z^2)\delta j_X + X^2\delta j_X \\ &- XY\delta j_Y - XZ\delta j_Z],\end{aligned} \tag{B6}$$

$$\begin{aligned}\mathcal{M}^{|K|=1}_{\mathrm{CD}}(\boldsymbol{r}_{\mathrm{int}}) = \frac{-i}{20c}\sqrt{\frac{3}{\pi}}[&-(Y^2+Z^2)\delta j_X - 3X^2\delta j_X \\ &- 2XY\delta j_Y - 2XZ\delta j_Z],\end{aligned} \tag{B7}$$

where $\boldsymbol{r}_{\mathrm{int}} = (X,Y,Z)$. We call $\mathcal{M}_{\mathrm{TD(CD)}}$ the TD(CD) transition density. For $j_Y = 0$ case, the TD and CD transition densities at $Y=0$ are written as

$$\begin{aligned}\mathcal{M}^{K=0}_{\mathrm{TD}}(X,0,Z) &= \frac{-i}{20c}\sqrt{\frac{3}{\pi}} \\ &\quad \times (2X^2\delta j_Z + Z^2\delta j_Z - ZX\delta j_X),\end{aligned} \tag{B8}$$

$$\begin{aligned}\mathcal{M}^{K=0}_{\mathrm{CD}}(X,0,Z) &= \frac{-i}{20c}\sqrt{\frac{3}{\pi}} \\ &\quad \times (-X^2\delta j_Z - 3Z^2\delta j_Z - 2ZX\delta j_X),\end{aligned} \tag{B9}$$

$$\begin{aligned}\mathcal{M}^{|K|=1}_{\mathrm{TD}}(X,0,Z) &= \frac{-i}{20c}\sqrt{\frac{3}{\pi}} \\ &\quad \times (2Z^2\delta j_X + X^2\delta j_X - XZ\delta j_Z),\end{aligned} \tag{B10}$$

$$\begin{aligned}\mathcal{M}^{|K|=1}_{\mathrm{CD}}(X,0,Z) &= \frac{-i}{20c}\sqrt{\frac{3}{\pi}} \\ &\quad \times (-Z^2\delta j_X - 3X^2\delta j_X - 2XZ\delta j_Z).\end{aligned} \tag{B11}$$

APPENDIX C: VECTOR SPHERICAL HARMONICS

For given vectors $\boldsymbol{a}$ and $\boldsymbol{b}$,

$$\hat{\boldsymbol{a}}\cdot\boldsymbol{Y}_{\lambda L\mu}(\hat{\boldsymbol{b}}) = \sqrt{\frac{4\pi}{3}}[Y_L(\hat{\boldsymbol{b}})\otimes Y_1(\hat{\boldsymbol{a}})]_{\lambda\mu}, \tag{C1}$$

$$\begin{aligned}[Y_L(\hat{\boldsymbol{b}})\otimes Y_l(\hat{\boldsymbol{a}})]_{\lambda\mu} &\equiv \sum_{M,m}\langle LMlm|\lambda\mu\rangle \\ &\quad \times Y_{LM}(\hat{\boldsymbol{b}})Y_{lm}(\hat{\boldsymbol{a}}).\end{aligned} \tag{C2}$$

Explicit expressions of $\boldsymbol{a}\cdot[r^{\lambda+1}\boldsymbol{Y}_{\lambda L\mu}(\hat{\boldsymbol{r}})]$ for $\lambda=1$ and $\mu=0$ are

$$\begin{aligned}\boldsymbol{a}\cdot[r^2\boldsymbol{Y}_{100}(\hat{\boldsymbol{r}})] &= \sqrt{\frac{4\pi}{3}}ar^2Y_{00}(\hat{\boldsymbol{r}})Y_{10}(\hat{\boldsymbol{a}}) \\ &= \frac{1}{\sqrt{4\pi}}(x^2+y^2+z^2)a_z,\end{aligned} \tag{C3}$$

$$\begin{aligned}\boldsymbol{a}\cdot[r^2\boldsymbol{Y}_{120}(\hat{\boldsymbol{r}})] &= \sqrt{\frac{4\pi}{3}}ar^2\Bigg[\sqrt{\frac{3}{10}}Y_{21}(\hat{\boldsymbol{r}})Y_{1-1}(\hat{\boldsymbol{a}}) \\ &\quad - \sqrt{\frac{2}{5}}Y_{20}(\hat{\boldsymbol{r}})Y_{10}(\hat{\boldsymbol{a}}) \\ &\quad + \sqrt{\frac{3}{10}}Y_{2-1}(\hat{\boldsymbol{r}})Y_{11}(\hat{\boldsymbol{a}})\Bigg] \\ &= \frac{1}{\sqrt{8\pi}}(x^2a_z + y^2a_z - 2z^2a_z \\ &\quad - 3yza_y - 3zxa_x).\end{aligned} \tag{C4}$$

We define the x component

$$\boldsymbol{Y}_{1Lx}(\hat{\boldsymbol{r}}) \equiv -\tfrac{1}{2}[\boldsymbol{Y}_{1L1}(\hat{\boldsymbol{r}}) - \boldsymbol{Y}_{1L-1}(\hat{\boldsymbol{r}})] \tag{C5}$$

and get similar expressions as

$$\boldsymbol{a}\cdot[r^2\boldsymbol{Y}_{10x}(\hat{\boldsymbol{r}})] = \frac{1}{\sqrt{4\pi}}(x^2+y^2+z^2)a_x, \tag{C6}$$

$$\begin{aligned}\boldsymbol{a}\cdot[r^2\boldsymbol{Y}_{12x}(\hat{\boldsymbol{r}})] = \frac{1}{\sqrt{8\pi}}(&y^2a_x+z^2a_x-2x^2a_x\\ &-3zxa_z-3xya_y).\end{aligned} \tag{C7}$$

Here, we follow the transformation of the basis set $(x,y,z)\rightarrow(1,0,-1)$,

$$\boldsymbol{e}_1 \equiv -\tfrac{1}{2}(\boldsymbol{e}_x+i\boldsymbol{e}_y),\quad \boldsymbol{e}_0\equiv\boldsymbol{e}_z,\quad \boldsymbol{e}_{-1}\equiv\tfrac{1}{2}(\boldsymbol{e}_x-i\boldsymbol{e}_y), \tag{C8}$$

leading to the relation

$$\begin{aligned}a_1 &= -\tfrac{1}{2}(a_x+ia_y),\\ a_0 &= a_z,\\ a_{-1} &= \tfrac{1}{2}(a_x-ia_y),\end{aligned} \tag{C9}$$

and its inverse relation

$$a_x = -\frac{1}{2}(a_1-a_{-1}),\quad a_y=\frac{i}{2}(a_1+a_{-1}),\quad a_z=a_0. \tag{C10}$$

APPENDIX D: MATRIX ELEMENTS OF DIPOLE OPERATORS FOR AMD WAVE FUNCTION

For the single-particle operator of the the current density

$$\boldsymbol{j}_{\rm sp}(\boldsymbol{r}) \equiv -\frac{i\hbar}{2m}\nabla_k\delta(\boldsymbol{r}-\boldsymbol{r}_k)+\delta(\boldsymbol{r}-\boldsymbol{r}_k)\nabla_k, \tag{D1}$$

the matrix element for single-particle wave functions of the AMD wave function is given as

$$\begin{aligned}\langle\varphi_i|\boldsymbol{j}_{\rm sp}(\boldsymbol{r})|\varphi_j\rangle &= \frac{\hbar}{m}\boldsymbol{K}_{ij}\phi^*_{\boldsymbol{X}_i}(\boldsymbol{r})\phi_{\boldsymbol{X}_j}(\boldsymbol{r})\\ &\quad\times\langle\chi_i|\chi_j\rangle\langle\tau_i|\tau_j\rangle,\end{aligned} \tag{D2}$$

$$\boldsymbol{K}_{ij} \equiv -i\sqrt{\nu}(\boldsymbol{X}_i^*-\boldsymbol{X}_j), \tag{D3}$$

and the matrix element of $\boldsymbol{j}_{\rm sp}(\boldsymbol{r})\cdot[r^2\boldsymbol{Y}_{1L\mu}(\hat{\boldsymbol{r}})]$ is given as

$$\begin{aligned}&\langle\varphi_i|\boldsymbol{j}_{\rm sp}(\boldsymbol{r})\cdot[r^2\boldsymbol{Y}_{1L\mu}(\hat{\boldsymbol{r}})]|\varphi_j\rangle\\ &\quad=\sqrt{\frac{4\pi}{3}}R_{ij}^2K_{ij}[Y_L(\hat{\boldsymbol{R}}_{ij})\otimes Y_1(\hat{\boldsymbol{K}}_{ij})]_{1\mu}\\ &\qquad\times\phi^*_{\boldsymbol{X}_i}(\boldsymbol{r})\phi_{\boldsymbol{X}_j}(\boldsymbol{r})\langle\chi_i|\chi_j\rangle\langle\tau_i|\tau_j\rangle,\end{aligned} \tag{D4}$$

$$\boldsymbol{R}_{ij} \equiv \frac{1}{2\sqrt{\nu}}(\boldsymbol{X}_i^*+\boldsymbol{X}_j). \tag{D5}$$

[1] N. Paar, D. Vretenar, E. Khan, and G. Colo, Rept. Prog. Phys. **70**, 691 (2007).
[2] T. Aumann and T. Nakamura, Phys. Scr. T **152**, 014012 (2013).
[3] D. Savran, T. Aumann, and A. Zilges, Prog. Part. Nucl. Phys. **70**, 210 (2013).
[4] A. Bracco, F. C. L. Crespi, and E. G. Lanza, Eur. Phys. J. A **51**, 99 (2015).
[5] J. Endres, E. Litvinova, D. Savran, P. A. Butler, M. N. Harakeh, S. Harissopulos, R.-D. Herzberg, R. Krücken, A. Lagoyannis, N. Pietralla, V. Y. Ponomarev, L. Popescu, P. Ring, M. Scheck, K. Sonnabend, V. I. Stoica, H. J. Wörtche, and A. Zilges, Phys. Rev. Lett. **105**, 212503 (2010).
[6] V. Derya *et al.*, Phys. Lett. B **730**, 288 (2014).
[7] F. C. L. Crespi *et al.*, Phys. Rev. Lett. **113**, 012501 (2014).
[8] F. C. L. Crespi *et al.*, Phys. Rev. C **91**, 024323 (2015).
[9] N. Nakatsuka *et al.*, Phys. Lett. B **768**, 387 (2017).
[10] B. L. Berman and S. C. Fultz, Rev. Mod. Phys. **47**, 713 (1975).
[11] H. P. Morsch, M. Rogge, P. Turek, and C. Mayer-Böricke, Phys. Rev. Lett. **45**, 337 (1980).
[12] M. N. Harakeh and A. E. L. Dieperink, Phys. Rev. C **23**, 2329 (1981).
[13] N. V. Giai and H. Sagawa, Nucl. Phys. A **371**, 1 (1981).
[14] G. Colo and G. N. Van, Nucl. Phys. A **731**, 15 (2004).
[15] P. Decowski, H. P. Morsch, and W. Benenson, Phys. Lett. B **101**, 147 (1981).
[16] T. D. Poelhekken, S. K. B. Hesmondhalgh, H. J. Hofmann, A. van der Woude, and M. N. Harakeh, Phys. Lett. B **278**, 423 (1992).
[17] G. Colo, N. Van Giai, P. F. Bortignon, and M. R. Quaglia, Phys. Lett. B **485**, 362 (2000).
[18] D. Vretenar, N. Paar, P. Ring, and T. Nikšić, Phys. Rev. C **65**, 021301(R) (2002).
[19] N. Ryezayeva, T. Hartmann, Y. Kalmykov, H. Lenske, P. von Neumann-Cosel, V. Y. Ponomarev, A. Richter, A. Shevchenko, S. Volz, and J. Wambach, Phys. Rev. Lett. **89**, 272502 (2002).
[20] P. Papakonstantinou, V. Y. Ponomarev, R. Roth, and J. Wambach, Eur. Phys. J. A **47**, 14 (2011).
[21] J. Kvasil, V. O. Nesterenko, W. Kleinig, P.-G. Reinhard, and P. Vesely, Phys. Rev. C **84**, 034303 (2011).
[22] A. Repko, P.-G. Reinhard, V. O. Nesterenko, and J. Kvasil, Phys. Rev. C **87**, 024305 (2013).
[23] V. O. Nesterenko, J. Kvasil, A. Repko, W. Kleinig, and P.-G. Reinhard, Phys. At. Nucl. **79**, 842 (2016).
[24] Y. Suzuki and S. Hara, Phys. Rev. C **39**, 658 (1989).
[25] T. Kawabata *et al.*, Phys. Lett. B **646**, 6 (2007).
[26] Y. Funaki, A. Tohsaki, H. Horiuchi, P. Schuck, and G. Ropke, Eur. Phys. J. A **28**, 259 (2006).
[27] Y. Kanada-En'yo, Phys. Rev. C **75**, 024302 (2007).
[28] T. Wakasa, E. Ihara, K. Fujita, Y. Funaki, K. Hatanaka, H. Horiuchi, M. Itoh, J. Kamiya *et al.*, Phys. Lett. B **653**, 173 (2007).
[29] T. Yamada, Y. Funaki, T. Myo, H. Horiuchi, K. Ikeda, G. Ropke, P. Schuck, and A. Tohsaki, Phys. Rev. C **85**, 034315 (2012).
[30] T. Ichikawa, N. Itagaki, T. Kawabata, T. Kokalova, and W. von Oertzen, Phys. Rev. C **83**, 061301(R) (2011).
[31] T. Kawabata *et al.*, J. Phys. Conf. Ser. **436**, 012009 (2013).
[32] Y. Kanada-En'yo, Phys. Rev. C **89**, 024302 (2014).
[33] Y. Kanada-En'yo, Phys. Rev. C **93**, 054307 (2016).
[34] Y. Chiba and M. Kimura, Phys. Rev. C **91**, 061302(R) (2015).
[35] Y. Chiba, M. Kimura, and Y. Taniguchi, Phys. Rev. C **93**, 034319 (2016).
[36] Y. Chiba, Y. Taniguchi, and M. Kimura, Phys. Rev. C **95**, 044328 (2017).

[37] M. Kimura, Phys. Rev. C **95**, 034331 (2017).

[38] B. John, Y. Tokimoto, Y.-W. Lui, H. L. Clark, X. Chen, and D. H. Youngblood, Phys. Rev. C **68**, 014305 (2003).

[39] Y.-W. Lui, H. L. Clark, and D. H. Youngblood, Phys. Rev. C **64**, 064308 (2001).

[40] W. von Oertzen, M. Freer, and Y. Kanada-En'yo, Phys. Rep. **432**, 43 (2006).

[41] M. Freer, Rep. Prog. Phys. **70**, 2149 (2007).

[42] Y. Kanada-En'yo, M. Kimura, and A. Ono, Prog. Theor. Exp. Phys. **2012**, 01A202 (2012).

[43] M. Ito and K. Ikeda, Rep. Prog. Phys. **77**, 096301 (2014).

[44] M. Ito, Phys. Rev. C **83**, 044319 (2011).

[45] Y. Kanada-En'yo, Phys. Rev. C **94**, 024326 (2016).

[46] Y. Kanada-En'yo, Phys. Rev. C **93**, 024322 (2016).

[47] A. Ono, H. Horiuchi, T. Maruyama, and A. Ohnishi, Phys. Rev. Lett. **68**, 2898 (1992).

[48] A. Ono, H. Horiuchi, T. Maruyama, and A. Ohnishi, Prog. Theor. Phys. **87**, 1185 (1992).

[49] Y. Kanada-En'yo, H. Horiuchi, and A. Ono, Phys. Rev. C **52**, 628 (1995).

[50] Y. Kanada-En'yo and H. Horiuchi, Phys. Rev. C **52**, 647 (1995).

[51] Y. Kanada-En'yo and H. Horiuchi, Prog. Theor. Phys. Suppl. **142**, 205 (2001).

[52] V. M. Dubovik and A. A. Cheshkov, Sov. J. Part. Nucl. **5**, 318 (1974).

[53] S. F. Semenko, Sov. J. Nucl. Phys. **34**, 356 (1981).

[54] D. G. Ravenhall and J. Wambach, Nucl. Phys. A **475**, 468 (1987).

[55] T. Ando, K. Ikeda, and A. Tohsaki, Prog. Theor. Phys. **64**, 1608 (1980).

[56] R. Tamagaki, Prog. Theor. Phys. **39**, 91 (1968).

[57] N. Yamaguchi, T. Kasahara, S. Nagata, and Y. Akaishi, Prog. Theor. Phys. **62**, 1018 (1979).

[58] Y. Kanada-En'yo, Phys. Rev. Lett. **81**, 5291 (1998).

[59] Y. Kanada-En'yo, H. Horiuchi, and A. Dote, Phys. Rev. C **60**, 064304 (1999).

[60] Y. Kanada-En'yo, Prog. Theor. Phys. **117**, 655 (2007); **121**, 895 (2009).

[61] N. Itagaki and S. Okabe, Phys. Rev. C **61**, 044306 (2000).

[62] C. M. Mattoon, F. Sarazin, C. Andreoiu, A. N. Andreyev, R. A. E. Austin, G. C. Ball, R. S. Chakrawarthy, D. Cross, E. S. Cunningham, J. Daoud, P. E. Garrett, G. F. Grinyer, G. Hackman, D. Melconian, C. Morton, C. Pearson, J. J. Ressler, J. Schwarzenberg, M. B. Smith, and C. E. Svensson, Phys. Rev. C **80**, 034318 (2009).